JOURNAL OF AIRCRAFT
Vol. 46, No. 3, May–June 2009

Experimental Investigation of Annular Wing Aerodynamics

Lance W. Traub*
Embry-Riddle Aeronautical University, Prescott, Arizona 86301

DOI: 10.2514/1.39822

A low-speed wind-tunnel investigation was conducted to explore the behavior of annular (ring) wings. Effects of aspect ratio as well as gap were investigated. Ring wings using a low Reynolds number Eppler section and a NACA 0012 profile were manufactured and tested. Measurements were recorded using a six-component sting balance. Experimental and theoretical trend comparisons were effected using a vortex-lattice code. The experimental results indicate wing efficiency factors well above 1 are achievable. The effect of gap was to increase the wing lift-curve slope as well as efficiency. The large increases in aerodynamic efficiency were generally mitigated by the significant minimum drag coefficient. Pitching moment characteristics were unfavorable and were dominated by dissimilar stall behavior between the upper and lower wing sections.

Introduction

THE benefits of wing nonplanarity are well known and were elucidated theoretically and experimentally soon after the inception of detailed aerodynamic understanding. Both Prandtl and Tietjens [1] and Munk [2] investigated the physics and determined theoretical calculation methods for nonplanar wings in the form of biplanes. The dawn of aviation saw the widespread use of nonplanar wings; however, this was more to do with structural expediency than augmented aerodynamic efficiency. Nonplanarity for a confined wing span may improve wing efficiency by capturing a larger volume of air to generate the lift impulse. Consequently, the downwash at a point is reduced [3] as trailing vorticity is displaced from the plane of the wing.

The most visible nonplanar implementation is the end plate [4] or its developed embodiment, the winglet [5,6]. Winglets reduce induced drag by redistributing the spanwise load so that it is reduced at the root and increased outboard, with the result that the downwash over the wing is still constant if optimal, but of reduced magnitude. An optimally loaded winglet that is perpendicular to the wing plane has zero net normal wash. Although efficient in an inviscid analysis, the significant junction flow drag increase associated with the confluence of the wing and end-plate boundary layers generally mitigated implementation for efficiency gain. Wings that are designed integrally for winglets show greatly diminished junction flow issues as opposed to retrofitted wings.

A study by Lowson [7] indicated that spanwise nonplanarity is most effective when implemented primarily near the wing tip. Thus, for a fixed wing-tip height and span, a simple end-plate implementation would yield efficiency superior to a circular or elliptic anhedral/dihedral distribution. When the wing span is not constrained, an increase in wing span will generally yield a preferable efficiency increase to a corresponding nonplanar increase if it is desired to improve efficiency. However, the corresponding increase in structural weight (which may be mitigated using composite structure or load-alleviation effectors) can decrease the benefit. For a fixed-wing-root bending moment, higher inboard load is desirable. Although this reduces the wing's efficiency, the increase in allowable span (while constraining moment) more than compensates to reduce drag. Theoretically, both positive or negative spanwise camber (i.e., up or down) will yield essentially equal efficiency augmentation. However, the lift-curve slope may vary with upward spanwise camber (dihedral), showing a greater lift-curve slope, due to so-called induced lift [3]. This may be interpreted as the effect of the orientation of the bound-vortex elements; their induced velocity augments the freestream for dihedral.

Closed nonplanar wings in the form of both annular (ring) or box wings have also been investigated theoretically [8–10] and experimentally [11]. The theoretical maximum spanwise efficiency for an unswept planar wing of fixed span that corresponds to elliptic loading is 1, a result determined by Munk [12]. This condition corresponds to uniform downwash in the assumed rigid wake. Analysis of annular wings shows a span efficiency (or Oswald) factor of $e = 2$. For a similar span, height, and required lift coefficient, a box wing has the lowest theoretical inviscid drag coefficient [13], with a computed value of $e = 2.78$. A biplane under similar conditions has a value of $e = 1.64$ and tends to $e = 2$ with infinite wing spacing. The limited use of these forms of wings may, in part, be due to structural complexity as well as a significant zero-lift drag coefficient penalty caused by the increase in wetted area over the comparative planar wing. A regime in which nonplanarity would be of benefit would be that in which span is limited and flight operation is at high load [i.e., for a loitering unmanned aerial vehicle (UAV) or a micro-UAV-type vehicle].

A survey of the literature shows little published data for annular wings in general and none at low Reynolds numbers. This wing form was implemented (not entirely successfully) in the French Atar Volant Coleopter [14], an aircraft designed for vertical takeoff. However, stability and control issues mitigated successful implementation. Annular wings have seen implementation as propeller shrouds in some micro UAV designs [15].[†] Fletcher [11] investigated the longitudinal characteristics of five annular wings of $AR = \frac{1}{3}, \frac{2}{3}, 1$, 1.5, and 3 equipped with Clark Y sections. The Reynolds number varied from 0.7×10^6 to 2.1×10^6 (as the model chord varied). The results indicated that the lift-curve slope of an annular wing is approximately twice that of the projected planar wing of span equal to the wing's diameter. Drag polar comparisons indicated reasonable agreement between experiment and theory with e assumed as 2. Note that the reference area used in [11] was that of the inner diameter of the ring wing multiplied by the chord.

Although application is obvious, the lack of available information concerning annular wing operation at low Reynolds numbers prompted the present investigation. A complicating factor is the poor performance of most airfoils at low Reynolds numbers. Typically, a symmetrical section does not perform well at low Reynolds numbers. Additionally, a cambered profile implemented in an annular wing may result in degraded performance due to the lower wing section operating inverted for positive angles of attack. Consequently, in this

---

Received 16 July 2008; revision received 30 October 2008; accepted for publication 31 October 2008.

*Associate Professor, Aerospace and Mechanical Engineering Department. Member AIAA.

[†] Data available online at http://www.aurora.aero/TacticalSystems/GoldenEye50.aspx [retrieved 23 June 2008].

study, an Eppler 68 (E-68) low Reynolds number section was merged into a NACA 0012 at the sides of the ring to facilitate a smooth transition where the wing was joined. This allowed both the upper and lower wing sections to be run such that the airfoil sections, where tested, were normal. Additionally, a similar wing using a NACA 0012 profile was also manufactured and tested. Results are presented showing the effects of aspect ratio and gap on measured coefficients. Comparisons with a vortex-lattice code are also included. This paper presents a detailed and systematic study of the behavior of annular wings at low Reynolds numbers.

Equipment and Procedure

Wind-tunnel tests were conducted in Embry-Riddle's 2 by 2 ft blower wind tunnel. This facility has a measured turbulence intensity of 0.5% and a jet uniformity within 1% in the jet core. Force-balance measurements were undertaken using a 6-component NK biotechnical sting balance. A dedicated interface coded in Visual Basic 6 was written for this balance. Balance output voltages were digitized using a National Instruments 16-bit A/D board. Voltages were converted to loads using an internal calibration matrix. Each presented data point is the average of 5000 readings. The acquisition code also has the ability to establish uncertainty intervals by acquiring 50 samples of the 5000 reading averages. These are then used to calculate the 95.5 or 99.7% probability interval of the mean. Before testing, the balance's calibration was checked through the application of known weights.

The model's angle of attack was set and measured using a feedback loop in conjunction with a Midori angle sensor. Angle-of-attack repeatability was established as better than 0.1 deg. Wall corrections were applied using the method of Shindo [16] as well as that detailed in [17]. Wind-tunnel testing was conducted at a freestream velocity of 40 m/s, yielding a Reynolds number of 225,000 based on the reference chord length of 0.1 m. During testing, the models were pitched from −6 to 28 deg in 2 deg increments.

The wind-tunnel models were rapid-prototyped from acrylonitrile butadiene styrene using Embry-Riddle's rapid-prototyping facilities. All wings had a chord of 0.1 m. Three models were manufactured: an $AR = 1$ annular wing with a merged E-68 and NACA 0012 profile, an $AR = 2$ annular wing that was split into two sections so that the effect of gap could be investigated (using a merged E-68 and NACA 0012 section), and a split $AR = 2$ NACA 0012 sectioned annular wing. The merged section wings used the NACA 0012 profile in the last 10% of the wing-tip region so that the wings had a smooth junction when joined. Consequently, the Eppler profiled wings possessed moderate aerodynamic washout. A rendering and photographs showing model installation are shown in Fig. 1. Presented coefficients are based upon a reference area corresponding to the wing's projected area. Moments are taken about the wing's quarter-chord. No boundary-layer transition devices (trip strips) were used. Surface flow visualization was undertaken using tufts attached to the suction surface of the annular (ring) wings to elucidate regions of attached and separated flows.

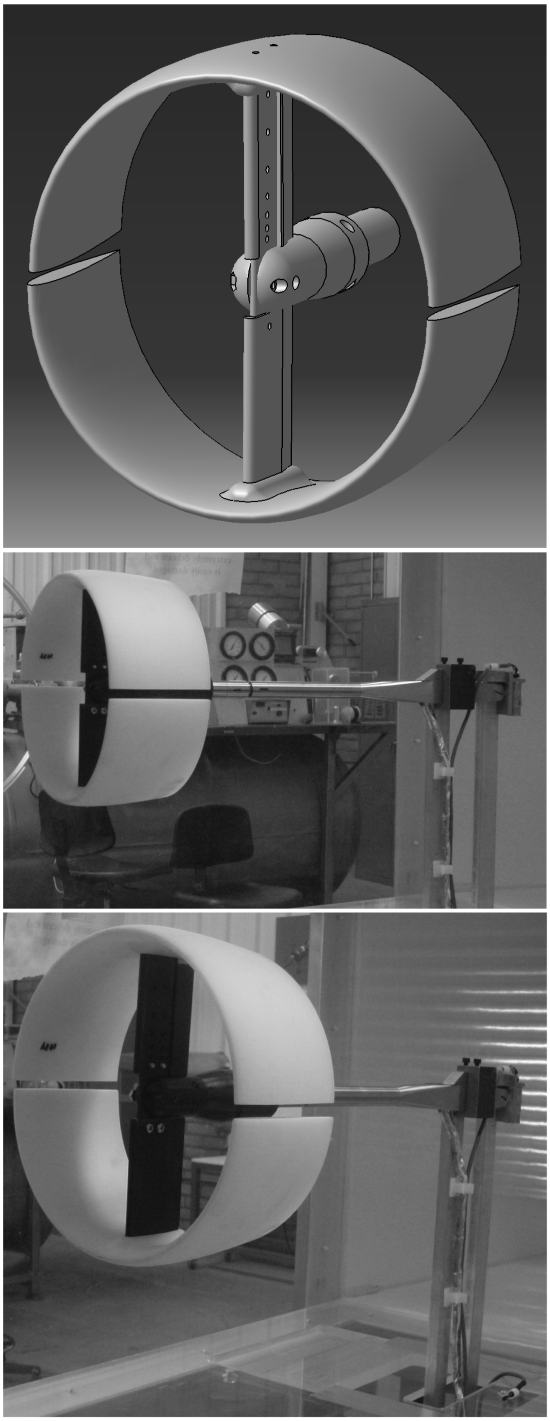

Fig. 1 $AR = 2$ model rendering and installation.

Results and Discussion

Repeatability of the data measurements is shown in Fig. 2 for data runs of the $AR = 2$ E-68 ring wing. The data sets were acquired over three consecutive days, indicated as run 1, run 2, and run 3. As may be seen, data repeatability is excellent. The top inset figure shows 99.7% probability intervals of the mean of the indicated coefficient calculated using 50 averaged data sets by the acquisition code. Evidently, the intervals are negligible, except in the poststall regime.

Effect of Aspect Ratio: Merged E-68–NACA 0012 Section

Comparisons of the $AR = 1$ and 2 ring wing (E-68—NACA 0012 section) are presented in Figs. 3–7. A lift coefficient comparison is indicated in Fig. 3. In this paper, numerical comparisons with the experiment have been implemented using the Athena vortex-lattice (AVL) code.[‡] The paneling was set to yield a total of 1600 panels with 10 chordwise and 80 spanwise on the upper and lower surfaces, respectively. The $AR = 2$ ring wing shows an experimental lift-curve slope of 0.071/deg compared with 0.078/deg from AVL (and 0.079/deg from Kalman et al. [18]). Note that a frequent correction to the two-dimensional lift-curve slope to account for viscous effects is to reduce it from 0.11 to 0.1/deg. This correction applied to the AVL data would bring the agreement between theory and experiment within 1%. The $AR = 1$ ring wing shows a linear curve until stall, without the gradual rounding before stall associated with the progression of separation from the trailing edge forward as seen in the other two data series. Stall is also seen to be delayed

---

[‡] Data available online at http://web.mit.edu/drela/Public/web/avl/ [retrieved 17 May 2008].

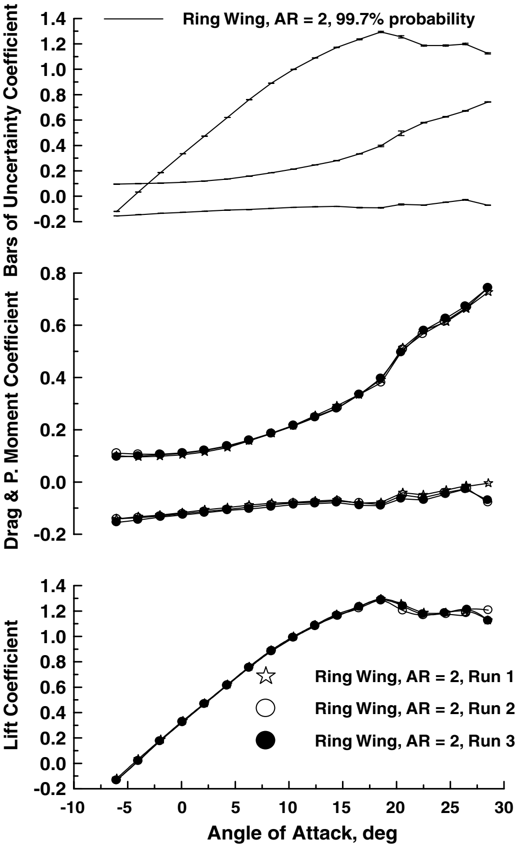

Fig. 2 Measurement repeatability and uncertainty intervals for a merged E-68—NACA 0012 section.

approximately 4 deg compared with the $\mathit{AR} = 2$ annular wing. Similar results are seen in the data of Fletcher [11]. This may be due to the low aspect ratio ($\mathit{AR} = 1$) causing a significant deflection of the stream tube through the wing's center, reducing loading on the lower wing and thereby delaying its stall. A theoretical analysis by Ribner [9] indicated a lift-curve slope for a high-aspect-ratio annular wing as

$$C_{L\alpha} = \frac{2C_{l\alpha}}{1 + 2/\mathit{AR}} = \frac{4\pi}{1 + 2/\mathit{AR}} \tag{1}$$

where $C_{L\alpha}$ and $C_{l\alpha}$ are the wing and section lift-curve slopes, respectively, and the second expression uses the classic value of $2\pi/\text{rad}$ for the sectional lift-curve slope. This expression is instantly recognized as precisely twice the value given by lifting-line theory for a planar unswept wing of elliptic loading. To account for the finite chord of the ring wing, it may be suitable to incorporate a planform perimeter modification in the spirit of that suggested by Jones [19]. The correction in this context is interpreted as the projected perimeter of the semispan divided by the wing span. This would result in

$$\begin{aligned} C_{L\alpha} &= \frac{2C_{l\alpha}}{(1 + 2/\mathit{AR})(1 + c/b)} = \frac{4\pi}{(1 + 2/\mathit{AR})(1 + c/b)} \\ &= \frac{4\pi}{1 + (3/\mathit{AR}) + (2/\mathit{AR}^2)} \end{aligned} \tag{2}$$

for a rectangular projected planform, where c is the chord and b is the wing span. Using Eq. (2) to estimate the lift-curve slopes for the $\mathit{AR} = 1$ and 2 annular wings yields values of 0.037 and 0.073/ deg, which compare favorably with the experimental values of 0.04 and 0.071/ deg.

The drag polar for the two wings is shown in Fig. 4. The significant zero-lift drag of the annular wings is evident. However, this may, in part, be due to the indicated drag values including the drag associated with the mounting bracket. The lift-dependent drag efficiency may be estimated by linearizing the drag polar [i.e., plotting the drag coefficient vs the square of the lift coefficient (see Fig. 5)]. The slope of the resulting plot relates to the lift-dependent drag of the system. Note that both the planform (vortex) and sectional (pressure) drag components are indicated as both vary with the square of the lift coefficient. As may be seen, the reduced slope of the $\mathit{AR} = 2$ ring wing compared with the $\mathit{AR} = 1$ wing is immediately indicative of improved aerodynamic efficiency. This may be quantified by writing the drag polar as approximately

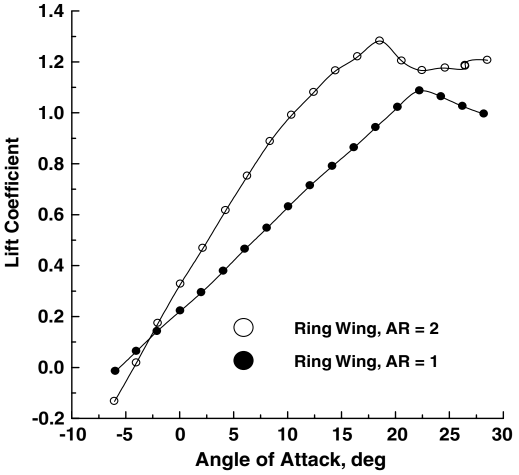

Fig. 3 Effect of aspect ratio and planform on the experimental lift coefficient.

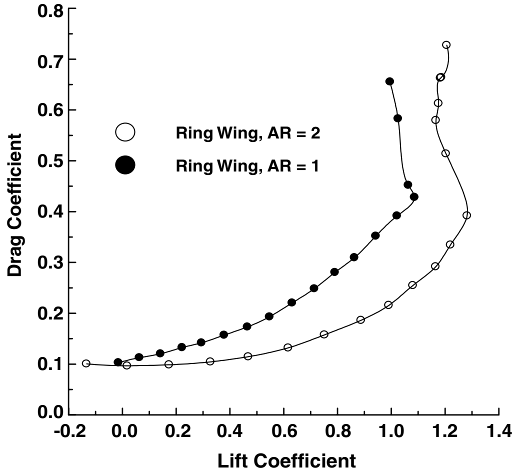

Fig. 4 Effect of aspect ratio and planform on the experimental drag coefficient.

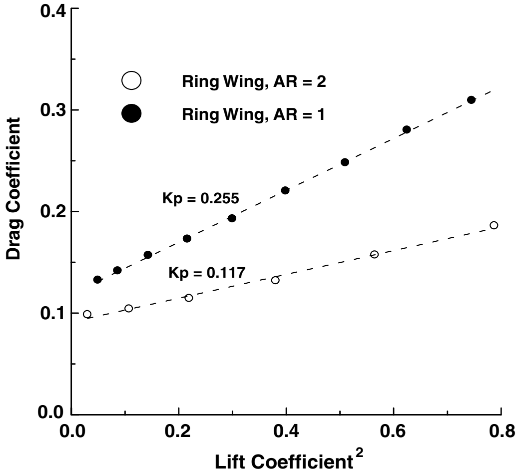

Fig. 5 Effect of aspect ratio and planform on the experimental linearized drag polar.

$$C_D = C_{D\min} + K_p C_L^2 = C_{D\min} + \frac{C_L^2}{\pi \mathit{AR} e} \qquad (3)$$

where C_D is the drag coefficient, $C_{D\min}$ is the minimum drag coefficient, C_L is lift coefficient, and K_p is the (essentially) pressure-based drag-due-to-lift factor. Thus, the K_p values indicated yield spanwise (including sectional) efficiency factors e of 1.36 for the $\mathit{AR} = 2$ ring wing and 1.25 for the $\mathit{AR} = 1$ ring wing. The inviscid efficiency for these wings is 2. The primary cause of the discrepancy is the drag contribution of the sectional pressure drag to the total drag. Consequently, the annular wings, with their large surface areas, also incur a large sectional drag penalty. Nonetheless, the efficiency factors are considerably higher than the planar theoretical maximum ($e = 1$).

The use of a linearized drag polar to ascertain wing efficiency results in an average efficiency for much of the angle-of-attack regime and assumes that the efficiency does not have a lift dependency. Although this is generally true for untwisted wings with attached flow, the present ring wings possess aerodynamic twist. Consequently, a plot of e as a function of lift coefficient shows efficiency variation through the incidence regime (see Fig. 6). As may be seen, the efficiency for the $\mathit{AR} = 1$ wing increases steadily and then plateaus from a lift coefficient of 0.5 to just before stall. The characteristics of the $\mathit{AR} = 2$ ring wing are different: the wing initially peaks with an e value close to the inviscid maximum, 2, indicating minimal sectional pressure drag contribution. The efficiency then drops steadily as the sectional drag grows and upper-surface separation manifests (as will be detailed later).

Longitudinal stability characteristics are explored in Fig. 7. The slope of the lines indicate that the aerodynamic center was ahead of the moment reference, the quarter-chord. Of interest are the moment breaks at stall. The $\mathit{AR} = 1$ ring wing initially shows a nose-up break followed by a nose-down (negative) moment break. The $\mathit{AR} = 2$ wing shows a nose-up moment stall. This suggests that the stall loads are associated to a greater extent with the wing configuration than the behavior of the sectional airfoil. As will be shown, the nose-up moment is due to the upper ring section stalling before the lower; hence, the significant drag differential causes a large nose-up moment break. It may also be seen in Figs. 3, 4, and 7 that a discontinuity in the behavior of the $\mathit{AR} = 1$ wing exists. At a lift coefficient of approximately 0.4, an increase in the wing's lift-curve slope, a change in the curvature of the drag polar, and a significant slope change in the pitching moment curve occur. The moment curve suggests a rearward movement of the wing's aerodynamic center that, in conjunction with the lift and drag increase, may suggest the onset of additional lift due to crossflow separation, as may be seen on slender cylinders at incidence.

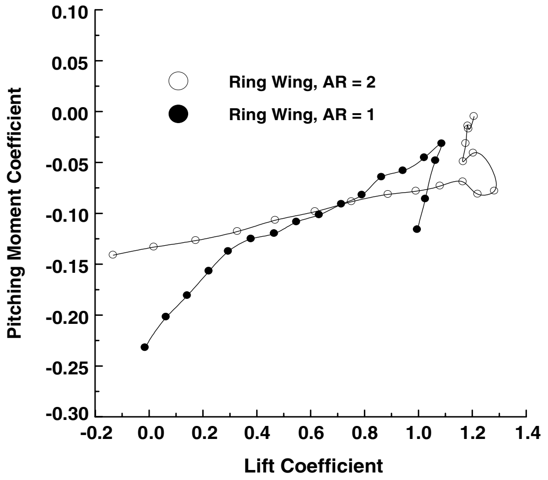

Fig. 7 Effect of aspect ratio and planform on the experimental pitching moment coefficient.

Effect of Wing Gap: Merged E-68–NACA 0012 Section

Figure 8 presents experimental results for a systematic variation of the gap between the upper and lower wing halves. As may be seen, increasing the gap causes an increase in the lift-curve slope, as the mutual influence of the wing sections on each other diminishes. Estimated lift-curve-slope values from the experimental data are 0.071/ deg (gap/$D = 0$), 0.075/ deg (gap/$D = 0.05$), 0.076/ deg (gap/$D = 0.11$), 0.079/ deg (gap/$D = 0.2$), 0.081/ deg (gap/$D =$ 0.33), and 0.084/ deg (gap/$D = 0.5$). The maximum lift coefficient also increases with gap. Stall characteristics show a weak but apparent dependence on the gap; increasing gap indicates a very docile stall, with stall followed by an extensive lift plateau of magnitude close to the maximum lift. Balance limitations precluded greater model incidence.

The effect of wing gap on the measured drag polar is explored in Fig. 9. The data show a systematic increase in the minimum drag coefficient with gap. This is most likely due to the design of the mount used to separate the wings. Wing separation unavoidably required greater exposure of the vertical supporting arms holding the wings. Consequently, the drag of the mount system also increased with gap, as reflected in the data. The significant zero-lift drag coefficient may mitigate the high aerodynamic efficiency. The greater curvature of the zero-gap polar indicates higher lift-dependent drag than the split-wing configurations; this is explored quantitatively in Fig. 10 with the linearized drag polar. K_p represents the slope of linear regression curve fits to the data sets. As may be seen, an increase in gap is associated with a reduction in the slope of the data

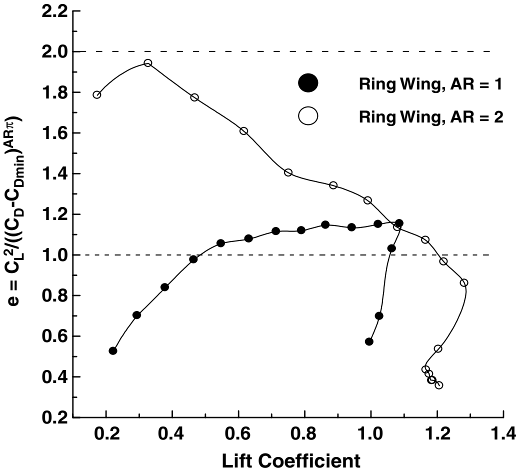

Fig. 6 Effect of aspect ratio and planform on the experimental variation of the efficiency factor with lift coefficient.

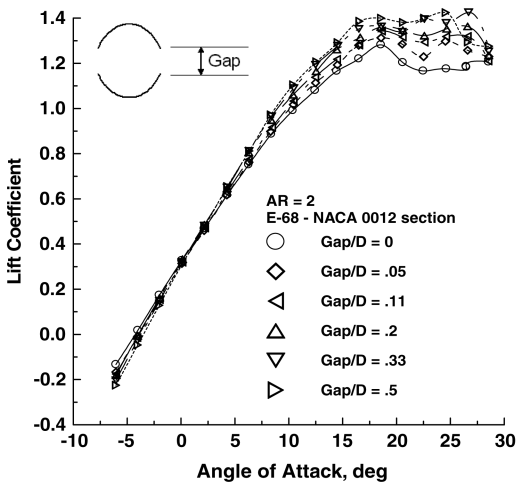

Fig. 8 Effect of gap on the measured lift coefficient for a merged E-68—NACA 0012 section.

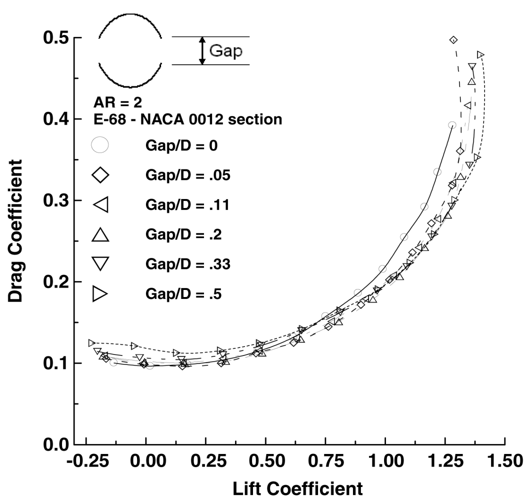

Fig. 9 Effect of gap on the measured drag coefficient for a merged E-68—NACA 0012 section.

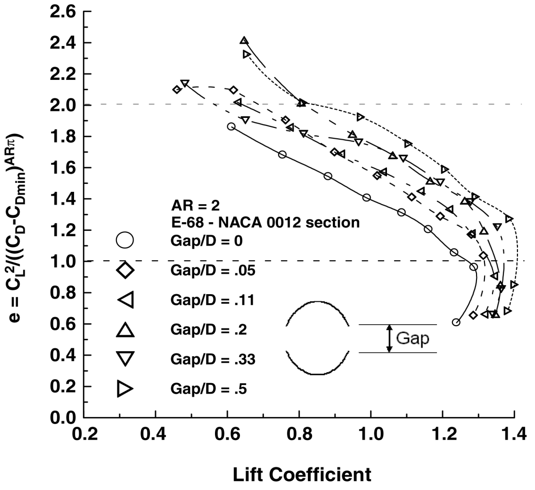

Fig. 11 Experimental variation of the efficiency factor with lift coefficient for a merged E-68—NACA 0012 section.

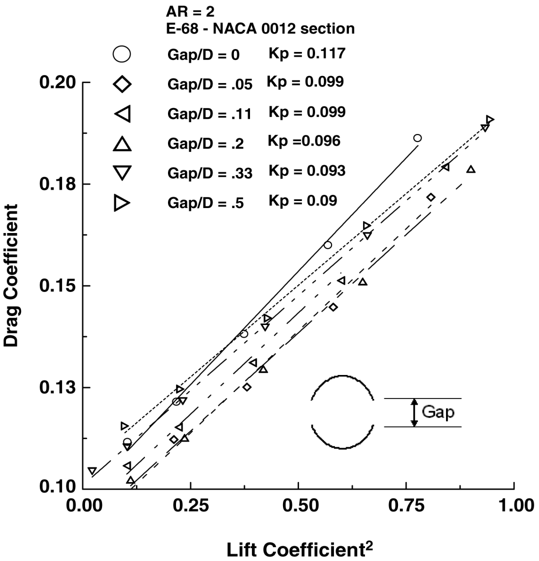

Fig. 10 Effect of gap on the measured linearized drag polar for a merged E-68—NACA 0012 section.

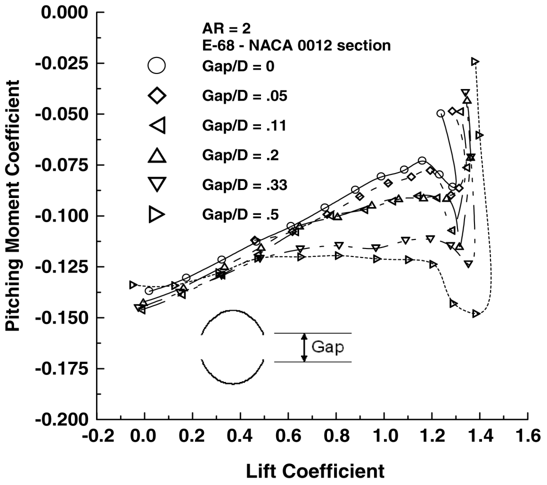

Fig. 12 Effect of gap on the measured pitching moment coefficient for a merged E-68—NACA 0012 section.

sets and consequently lift-dependent drag. This behavior is mathematically attributable to a reduction in the mutually induced downwash (from the trailing vortex systems) between the wings. Although the efficiency of aerodynamically twisted wings is dependent on the lift coefficient, an average estimate of e may be determined from the K_p values in Fig. 10. Estimated e values from the experimental data are 1.36 ($\text{gap}/D = 0$), 1.61 ($\text{gap}/D = 0.05$), 1.61 ($\text{gap}/D = 0.11$), 1.66 ($\text{gap}/D = 0.2$), 1.71 ($\text{gap}/D = 0.33$), and 1.76 ($\text{gap}/D = 0.5$).

The dependency of e on lift coefficient is investigated in Fig. 11. The data indicate a systematic reduction in efficiency with increasing lift coefficient, an effect of camber that results in a higher peak e, but a greater variance with lift coefficient than for a symmetrical sectioned wing. Values of e greater than 2 are indicated; infinite wing spacing would show an inviscid $e = 3$ for two spanwise circular-arc wing sections.

The effects of wing spacing on the measured pitching moment coefficient is shown in Fig. 12. The data indicate that increasing the wing gap affects the recorded moment significantly for lift coefficients greater than 0.4. This lift coefficient corresponds to the angle at which the wing is geometrically at approximately 0 deg angle of attack. Below a lift coefficient of 0.4, all data sets show that the aerodynamic center is in front of the wing's quarter-chord. At higher loading, the moment for the two largest gaps levels out, suggesting movement of the wings aerodynamic center to coincide with the quarter-chord. All gaps show two moment reversals at stall: an initial nose-down break followed by a nose-up (destabilizing) break. The nose-down break is common for airfoils stemming from the lack of pressure recovery over the aft suction surface associated with massive separation. A nose-up break is seen on delta wings due to lift loss over the aft wing sections caused by vortex breakdown. For these annular wings, the nose-up break is caused by differential stall of the upper and lower wing segments, the upper wing stalling before the lower wing half and thus incurring a significant drag increase.

A summary of the effects of wing gap on the measured lift-curve slope and efficiency factor is presented in Fig. 13. The lift-curve slope increases at a diminishing rate with increasing gap, indicative of the 1/gap relationship of the induced velocities associated with the trailing vortex system. The wing efficiency e appears to show the greatest sensitivity to gap as the wing is initially split. Increasing gap improves the wing efficiency, in essence, through a reduction in downwash that may be interpreted as the wing capturing a larger volume of air or the distance between the trailing vortex legs of the respective wings increasing.

Effect of Wing Gap: NACA 0012 Section

The Eppler profile was used in the initial study to limit the perceived impact of sectional pressure drag on the results due to the low Reynolds number test range, as well as to provide an indication

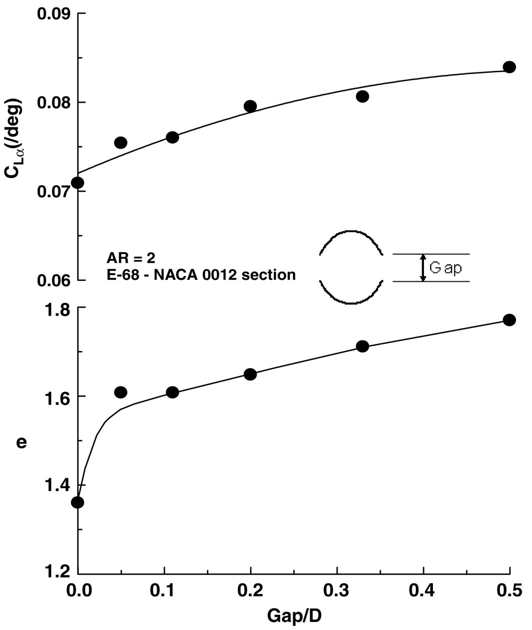

Fig. 13 Data summary showing the dependency of the wing lift-curve slope and average *e* on the gap for a merged E-68—NACA 0012 section.

of feasible performance. However, annular wings are usually implemented using symmetrical sections. Consequently, an additional $\mathcal{R} = 2$ annular wing was tested with a NACA 0012 section. As seen for the Eppler profiled wing, increasing the wing gap systematically increases the lift-curve slope (Fig. 14). Estimated lift-curve-slope values from the experimental data are 0.073/ deg ($\text{gap}/D = 0.04$), 0.076/ deg ($\text{gap}/D = 0.08$), 0.077/ deg ($\text{gap}/D = 0.15$), 0.081/ deg ($\text{gap}/D = 0.29$), 0.083/ deg ($\text{gap}/D = 0.35$), and 0.087/ deg ($\text{gap}/D = 0.52$). Stall characteristics indicate a moderate increase in the maximum lift coefficient with gap; however, the lift plateau observed in Fig. 8 is not evident.

Drag characteristics are explored in Figs. 15–17 in the form of the polar, linearized polar, and wing efficiency as a function of lift coefficient. As shown in Fig. 16, increasing gap reduces the slope of the linearized polars, reflecting diminished drag due to lift. Estimated *e* values from the experimental data are 1.26 ($\text{gap}/D = 0.04$), 1.32 ($\text{gap}/D = 0.08$), 1.42 ($\text{gap}/D = 0.15$), 1.46 ($\text{gap}/D = 0.29$), 1.55 ($\text{gap}/D = 0.35$), and 1.58 ($\text{gap}/D = 0.52$). The variation of the wing efficiency as a function of lift coefficient is presented in Fig. 17. Increasing gap yields an increase in the calculated efficiency. The lack of section camber is also reflected in the moderate invariance of *e* with lift coefficient over most of the attached-flow regime.

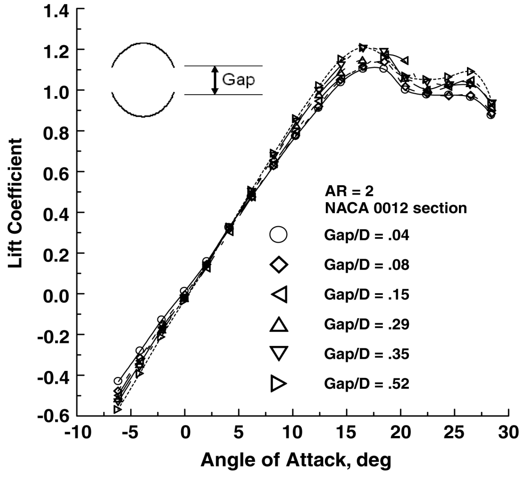

Fig. 14 Effect of gap on the measured lift coefficient for a NACA 0012 section.

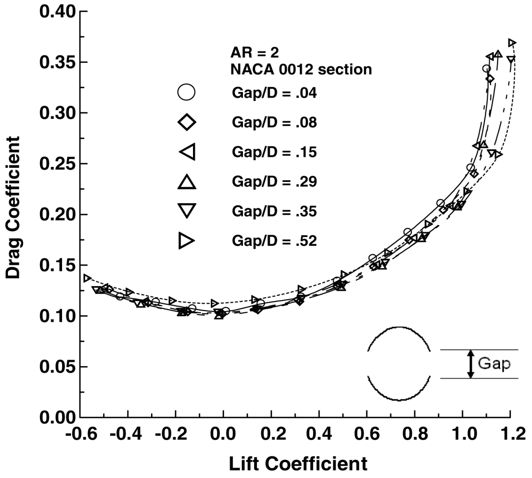

Fig. 15 Effect of gap on the measured drag coefficient for a NACA 0012 section.

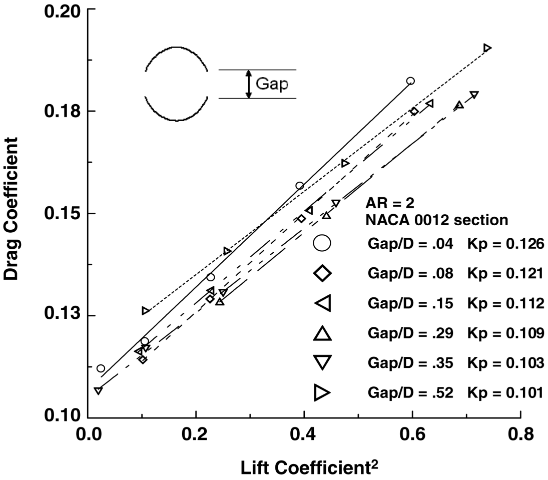

Fig. 16 Effect of gap on the measured linearized drag polar for a NACA 0012 section.

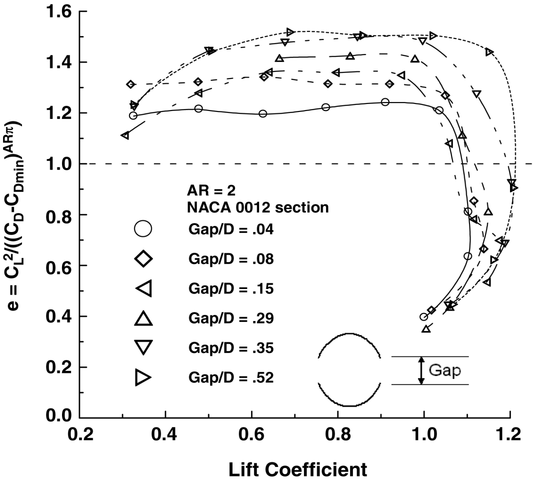

Fig. 17 Experimental variation of the efficiency factor with lift coefficient for a NACA 0012 section.

The pitching moment characteristics show similar trends (Fig. 18) to those for the cambered ring wing (Fig. 12). Notable is a divergence in the recorded moment with positive lift coefficient, such that increasing the gap decreases the nose-up moment, reflective of an aft movement of the aerodynamic center with increasing gap. The stall characteristics of the symmetrical wing are different from those

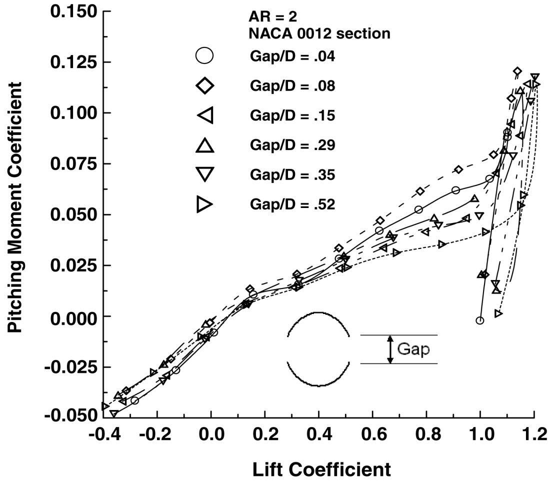

Fig. 18 Experimental variation of the measured pitching moment with lift coefficient for a NACA 0012 section.

observed for the cambered wing (Fig. 12). As may be seen in Fig. 18, the onset of stall shows a large nose-up moment (due to stall of the upper wing half) followed by a strong nose-down break as both the upper and lower sections stall.

Figure 19 displays a data summary indicating the effect of wing gap on the calculated wing lift-curve slope and efficiency factor. Estimates were also calculated using the vortex-lattice code AVL. It was found that the lift-curve slopes predicted by AVL were generally 9% higher than the experiment. Thus, for comparison of the effect of gap, the AVL data have been reduced accordingly, to afford shape comparison. As may be seen, agreement between the experiment and AVL for the dependency of the lift-curve slope on the gap is close. The lift-curve slope is most sensitive to the initial separation of the wing halves. The drag due to lift-efficiency factor is presented in the lower inset of Fig. 19. As found for the lift-curve slope, the initial separation of the wings shows the largest corresponding increase in wing efficiency.

The inviscid lift-curve slope and *e* dependencies as predicted by AVL are shown in Fig. 20. Effects of localized flow separation and the significant profile drag of the annular wing yield experimental values of *e* that are significantly lower than indicated in Fig. 20 (see Fig. 19). As shown, *e* values considerably greater than 2 can theoretically be achieved, with a calculated $e = 2.56$ for a gap of 0.5. Infinite wing separation would show $e = 3$. Theoretically, positive or negative spanwise camber has a negligible effect on *e*, but does affect the lift-curve slope. Considering the individual wings, upward curvature (dihedral) shows a higher lift-curve slope than downward (anhedral). This is due to so-called induced lift; that is, mathematically, this may be interpreted as an increase (or decrease) in axial velocity over the wing due to the influence of the bound vortices.

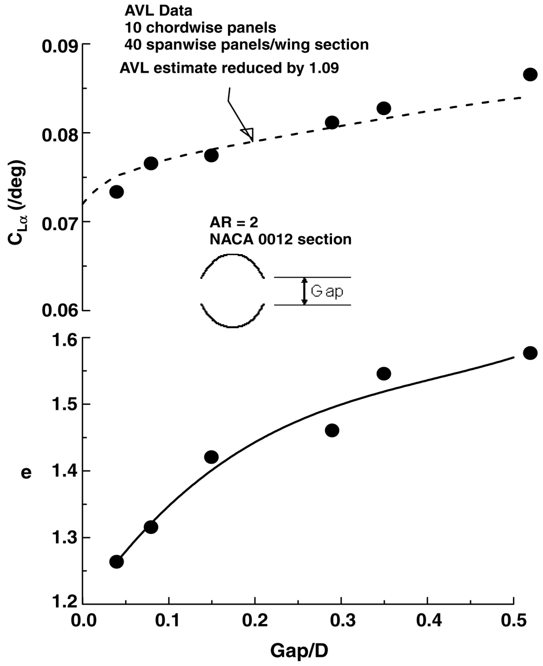

Fig. 19 Experimental data summary showing dependency of wing lift-curve slope and average *e* on the gap for a NACA 0012 section.

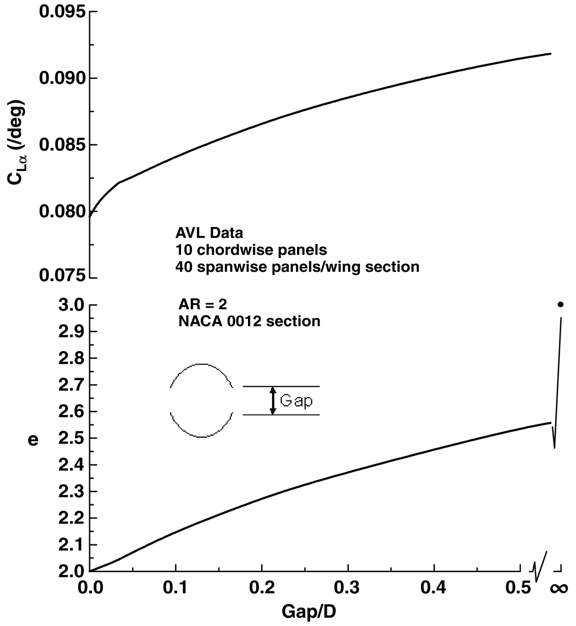

Fig. 20 Numerical estimate of the effect of gap on the wing lift-curve slope and inviscid spanwise efficiency factor.

Theoretical spanwise load distributions have also been explored using AVL. Figure 21 shows a screen capture of the paneling, wake, and loads for the $\mathrm{gap}/D = 0.52$ configuration. Although wake relaxation is not accounted for, this is unlikely to have a significant effect on the load estimates, as may be inferred from the success of lifting-line theory for high-aspect-ratio unswept wings. This is due to the wake, although not being force-free, being drag-free. Figure 22

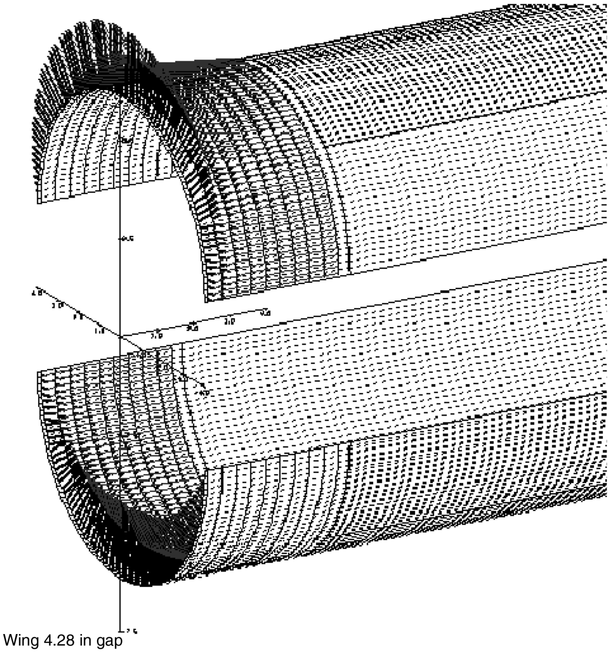

Fig. 21 AVL wing paneling. $\mathrm{gap}/D = 0.52$.

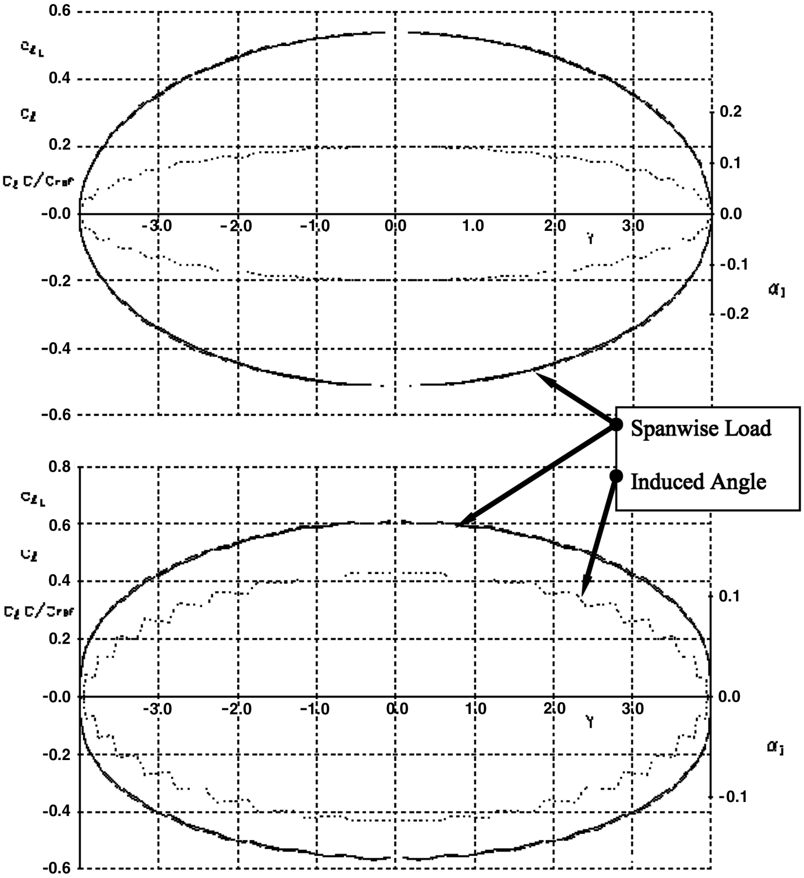

Fig. 22 AVL Trefftz plane spanwise load and normal wash distribution at AOA = 10 deg and Æ = 2: gap/$D = 0$ (top) and gap/$D = 0.52$ (bottom).

shows screen captures of the Trefftz plane projection of the spanwise load distribution and induced angle of attack. As may be seen, the load distribution for the upper and lower surfaces appears elliptical, as shown theoretically by Ribner [9]. The upper wing half is seen to carry heavier loading than the lower surface. This can be interpreted as the effect of the bound vortices on the respective wing elements; the lower wing induces a freestream-orientated component on the upper wing, and the upper wing induces an upstream velocity component on the lower wing. Note that this bound-vortex contribution does not affect the total lift or drag that the wing may produce, only the distribution between the upper and lower wing elements. However, the disparate loading distribution may affect the stall progression over the wings. Note that the induced angle of attack tends to zero near the wing tips. As shown by Munk [12] for spanwise cambered wings, drag is minimized when the normal wash is equal to a constant multiplied by the cosine of the local wing spanwise incidence (90 deg at the wing tip). Separating the wings shows the spanwise load distribution deviating from elliptical. Both the upper and lower wings show heavier loading near the tips, as is typically seen with large outboard spanwise camber (i.e., an end plate), as may be expected, considering the present configuration.

Surface Visualization Characteristics

Figures 23 and 24 show the evolution of separation over the suction surface of two annular wing configurations: gap/$D = 0$ and 0.52, as indicated by surface flow tufts. For the closed wing, a small area of localized separation was observed on the lower wing adjacent to the support mount and was presumably due to it. At an angle of attack (AOA) of 16 deg, a small region of separation was observed at the top of the wing. Increasing the incidence to 18 deg showed a rapid growth in the spanwise extent of this region. At AOA = 26 deg, the upper surface was essentially separated; however, the lower surface flow was still largely attached. These uneven stall characteristics are responsible for the large indicated nose-up pitching moment. At AOA = 28 deg, the lower surface also showed evidence of large-scale separation. The dissimilar stall characteristics may, in part, be a result of the uneven loading between the upper and lower wing sections. The effect of gap is shown in Fig. 24. The observed characteristics are analogous to those described for the closed wing,

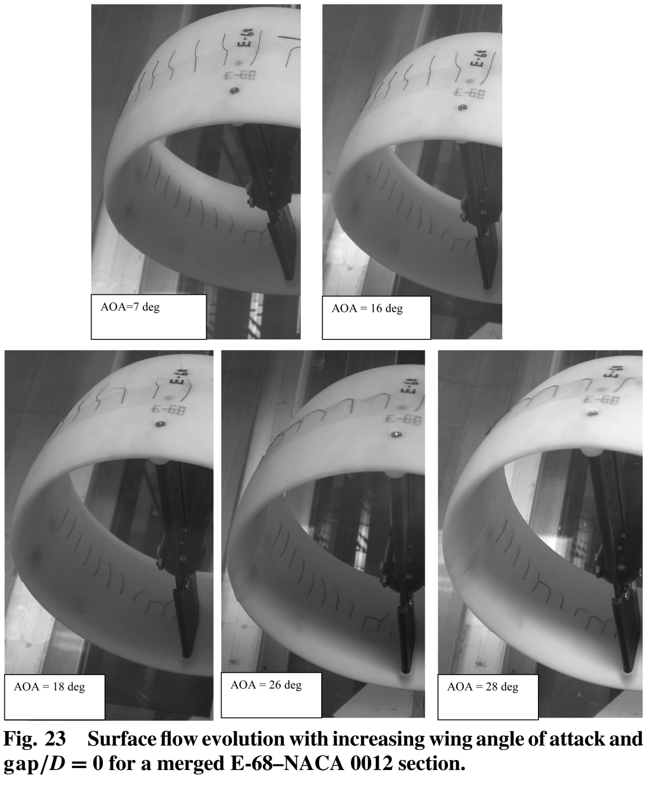

Fig. 23 Surface flow evolution with increasing wing angle of attack and gap/$D = 0$ for a merged E-68–NACA 0012 section.

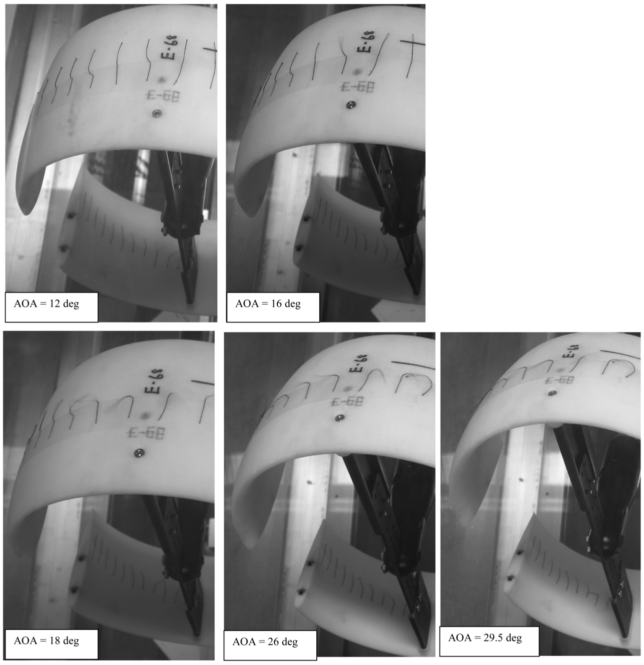

Fig. 24 Surface flow evolution with increasing wing angle of attack and $\mathbf{gap}/D = 0.52$ for a merged E-68—NACA 0012 section.

however, the onset of separation on the lower wing appeared to be delayed to a greater extent than for the closed wing.

The disparate stall characteristics observed may also be affected by the apparent sweep the wing(s) experience with incidence. This sweep results in a freestream velocity component in the spanwise direction (given by $U \sin\alpha \sin\phi$, where U is the freestream velocity, α is the angle of attack, and ϕ is the dihedral angle), with the magnitude of the component increasing toward the wing tip ($\phi \rightarrow \pm 90$ deg). Consequently, the wing has an apparent sweep$=\sin^{-1}(\sin\alpha \sin\phi)$. Additionally, when at incidence, the wing geometry causes a spanwise pressure gradient that drives boundary-layer migration, analogous to that present on planar swept wings. The lower wing would experience spanwise flow from the wing root to the tip, and this would have the effect of thickening the boundary layer near the tips in a similar fashion to a wing with aft sweep. Consequently, it may be expected that the tip region may separate first. However, the tip region is lightly loaded for a constant-chord annular wing (as opposed to an aft swept planar wing, on which the tip regions may be heavily loaded if not washed out), so that lower surface stall is greatly delayed. The upper section of the ring wing would experience spanwise flow from the wing tips to the root. This, in conjunction with the central region experiencing the highest loading, would cause stall at the root section first (similar to a forward swept wing), as observed in the tuft visualization.

Conclusions

An investigation into the behavior of continuous as well as split annular wings was conducted. Wind-tunnel tests were conducted at low Reynolds numbers (225,000) in a 2 by 2 ft blower tunnel. Forces and moment were measured using a 6-component sting balance. Numerical estimates of wing performance were calculated using a vortex-lattice code. Annular wings were manufactured with aspect ratios of 1 and 2. Two wing sections were used: a low Reynolds number Eppler profile and a NACA 0012. Results indicated reasonable agreement between theory and experiment in the behavior of the wing's lift-curve slope. The effect of gap was shown to increase the wing's lift-curve slope, as well as the drag, due to lift-efficiency factor. Stall characteristics were generally unfavorable due to stall of the upper wing section before the lower, resulting in a large nose-up moment. Although the annular wings demonstrated significant increases in wing efficiency compared with a planar wing with elliptic loading (with efficiencies well above 1 demonstrated), this was largely offset by the large minimum drag coefficient. The data suggest that annular wings may prove beneficial in flight regimes that encompass extended operation at high lift coefficients.

Acknowledgments

The author would like to thank Embry-Riddle Aeronautical University for support during the conduct of this study through an internal grant, as well as Jeff Walston, Chas Cooke, Julie Clark, and Joseph Lorkowski for the design and manufacture of the models. The author would also like to thank the Associate Editor and reviewers for their comments and suggestions.

References

[1] Prandtl, L., and Tietjens, O. G., *Applied Hydro and Aeromechanics*, Dover, New York, 1934, pp. 211–222.
[2] Munk, M. M., "General Biplane Theory," NACA Rept. 151, 1923.
[3] Cone, C. D., "The Theory of Induced Lift and Minimum Induced Drag on Non Planar-Lifting Systems," NASA TR-R-139, 1962.
[4] Hoerner, S. F., *Fluid-Dynamic Lift*, Hoerner Fluid Dynamics, Vancouver, WA, 1985, pp. 3–9.
[5] Maughmer, M. D., "The Design of Winglets for High-Performance Sailplanes," 19th AIAA Applied Aerodynamics Conference, Anaheim, CA, AIAA Paper 2001-2406, June 2001.
[6] Chattot, J. J., "Low-Speed Design and Analysis of Wing/Winglet Combinations Including Viscous Effects," *Journal of Aircraft*, Vol. 43, No. 2, 2006, pp. 386–389.
[7] Lowson, M. V., "Minimum Induced Drag for Wings with Spanwise Camber," *Journal of Aircraft*, Vol. 27, No. 7, 1990, pp. 627–631.
[8] Demasi, L., "Investigation on Conditions of Minimum Induced Drag of Closed Wing Systems and C-Wings," *Journal of Aircraft*, Vol. 44, No. 1, 2007, pp. 81–99.
[9] Ribner, H. S., "The Ring Airfoil in Nonaxial Flow," *Journal of Aeronautical Sciences*, Vol. 14, No. 9, 1947, pp. 529–530.
[10] Stewart, H. J., "The Aerodynamics of a Ring Airfoil," *Quarterly of Applied Mathematics*, July 1944, p. 136.
[11] Fletcher, H. S., "Experimental Investigation of Lift, Drag, and Pitching Moment of Five Annular Airfoils," NACA TN 4117, Oct. 1957.
[12] Munk, M., "The Minimum Induced Drag of Aerofoils," NACA Rept. 121, 1923.
[13] von Karman, T., and Burgers, J. M., *Aerodynamic Theory*, Vol. 2, Julius Springer, Berlin, 1943, p. 367.
[14] Bergaust, E., "The Coleopter—World's Most Radical Aircraft," *Aeronautical Digest*, Vol. 70, No. 6, June 1995, pp. 22–25.
[15] Morris, S. J., and Holden, M., "Design of Micro Air Vehicles and Flight Test Validation," *Proceedings of the Conference on Fixed, Flapping and Rotary Wing Vehicles at Very Low Reynolds Numbers*, 2000.
[16] Shindo, S., "Simplified Tunnel Correction Method," *Journal of Aircraft*, Vol. 32, No. 1, 1995, pp. 210–213.
[17] Barlow, J. B., Rae, W., and Pope, A., *Low-Speed Wind-Tunnel Testing*, 3rd ed., Wiley-Interscience, New York, 1999, pp. 367–425.
[18] Kalman, T. P., Rodden, W. P., and Giesing, J. P., "Application of the Doublet-Lattice Method to Nonplanar Configurations in Subsonic Flow," *Journal of Aircraft*, Vol. 8, No. 6, 1971, pp. 406–413.
[19] Jones, R. T., "Correction of the Lifting-Line Theory for the Effect of the Chord," NACA TN 817, 1941.